





Article

Wavelet Analysis of GPR Data for Belowground Mass Assessment of Sorghum Hybrid for Soil Carbon Sequestration

Matthew Wolfe ^{1,2,*}, Iliyana D. Dobрева ^{2,3} , Henry A. Ruiz-Guzman ², Da Huo ⁴ , Brody L. Teare ^{1,2}, Tyler Adams ^{1,2}, Mark E. Everett ⁵ , Michael Bishop ⁴, Russell Jessup ²  and Dirk B. Hays ^{1,2}

¹ Molecular and Environmental Plant Sciences, Texas A&M University, College Station, TX 77843, USA; blteare@tamu.edu (B.L.T.); tmadams13@gmail.com (T.A.); dbhays@tamu.edu (D.B.H.)

² Department of Soil and Crop Sciences, Texas A&M University, College Station, TX 77843, USA; dobrega.1@osu.edu (I.D.D.); henry.ruizguzman@ag.tamu.edu (H.A.R.-G.); rjessup@tamu.edu (R.J.)

³ Department of Geography, Ohio State University, Columbus, OH 43210, USA

⁴ Department of Geography, Texas A&M University, College Station, TX 77843, USA; daniel.huo@utoronto.ca (D.H.); michael.bishop@tamu.edu (M.B.)

⁵ Department of Geology and Geophysics, Texas A&M University, College Station, TX 77843, USA; everett@geo.tamu.edu

* Correspondence: mwolfe45@gmail.com

Abstract: Among many agricultural practices proposed to cut carbon emissions in the next 30 years is the deposition of carbon in soils as plant matter. Adding rooting traits as part of a sequestration strategy would result in significantly increased carbon sequestration. Integrating these traits into production agriculture requires a belowground phenotyping method compatible with high-throughput breeding (i.e., rapid, inexpensive, reliable, and non-destructive). However, methods that fulfill these criteria currently do not exist. We hypothesized that ground-penetrating radar (GPR) could fill this need as a phenotypic selection tool. In this study, we employed a prototype GPR antenna array to scan and discriminate the root and rhizome mass of the perennial sorghum hybrid PSH09TX15. B-scan level time/discrete frequency analyses using continuous wavelet transform were utilized to extract features of interest that could be correlated to the biomass of the subsurface roots and rhizome. Time frequency analysis yielded strong correlations between radar features and belowground biomass (max $R = -0.91$ for roots and -0.78 rhizomes, respectively) These results demonstrate that continued refinement of GPR data analysis workflows should yield an applicable phenotyping tool for breeding efforts in contexts where selection is otherwise impractical.

Keywords: ground-penetrating radar (GPR); continuous wavelet transform (CWT); wavelet pseudo-frequency (WPF); wavelet pseudo-frequency density (WPDF)



Citation: Wolfe, M.; Dobрева, I.D.; Ruiz-Guzman, H.A.; Huo, D.; Teare, B.L.; Adams, T.; Everett, M.E.; Bishop, M.; Jessup, R.; Hays, D.B. Wavelet Analysis of GPR Data for Belowground Mass Assessment of Sorghum Hybrid for Soil Carbon Sequestration. *Remote Sens.* **2023**, *15*, 3832. <https://doi.org/10.3390/rs15153832>

Academic Editor: Jeroen Meersmans

Received: 15 June 2023

Revised: 22 July 2023

Accepted: 31 July 2023

Published: 1 August 2023



Copyright: © 2023 by the authors. Licensee MDPI, Basel, Switzerland. This article is an open access article distributed under the terms and conditions of the Creative Commons Attribution (CC BY) license (<https://creativecommons.org/licenses/by/4.0/>).

1. Introduction

The global average temperature increased by 0.85 °C between 1880 and 2012. It is expected to reach 1.5 °C above preindustrial temperatures by 2040 [1]. Atmospheric concentrations of carbon dioxide are responsible for 20% of thermal energy absorbed by Earth's atmosphere [2], and the increase in atmospheric carbon and resulting warming due to the greenhouse effect has severe negative ramifications for many important ecological systems on a planet-wide scale. A viable strategy to achieve net-negative emissions is the recapture and storage of atmospheric carbon as recalcitrant plant mass. Among proposed plant materials, grass species have been suggested as efficient targets for sequestration efforts through the restoration and establishment of natural grasslands or improvement of the carbon sequestration potential of dominant cereal crops. Grasslands can sequester up to ~3 Mg of C per hectare per year [3], and also serve as a carbon sink in agricultural settings. Previous estimates predict that ~750 Mha are available globally for conversion to bioenergy cultivation, with an estimated sequestration potential of ~1600 Tg C y⁻¹ [4].

Furthermore, the addition of perennially conferring traits, such as rhizomes, to current grain crops, such as wheat, rice, barley, maize, sorghum, and millet, could increase their carbon sequestration potential several-fold compared to the current low biomass found in current fibrous root cereals.

A step toward optimizing carbon deposition via crop methods is the systematic study and refinement of root and rhizome traits through breeding. The scale needed by breeding strategies requires a fast and efficient means of phenotyping root traits; however, there is currently no method that meets these requirements. Maximizing belowground biomass necessitates developing high-throughput phenotyping methods for making rapid trait selection decisions in field trials. The current methods of root phenotyping in a field setting provide high-quality root information; however, some aspects of these methods are unattractive for plant breeders: they tend to be labor intensive, challenging due to inherent field variability, require a secondary cleaning of root samples, and are destructive [5]. Recent studies have shown that increasing the quantity of the acquired phenotypic data collected may reduce error, making high-throughput phenotyping an attractive alternative to manual phenotyping methods [6].

Ground-penetrating radar (GPR) is emerging as a potential high-throughput and non-destructive root phenotyping method. GPR is a geophysical technique that uses electromagnetic waves in the MHz–GHz frequency range to image subsurface structures. It operates by first sending a pulse of energy into the ground and then recording the resulting time-variations in the returned field amplitude caused by scattering, reflection, and diffraction of the pulse due to subsurface discontinuities in electromagnetic wave impedance. Beginning in the late 20th century, GPR has been used to monitor water flow through soil horizons [7], map bedrock [8], estimate soil depth [9], and track movement of agrochemicals [10].

Tree roots were among the first botanical targets studied, and given their large diameter, they are readily detected by GPR [11]. As such, the majority of early root studies using GPR are within the field of forestry. Beyond simple detection, forestry studies indicate the possibility of predicting both tree root biomass and architecture based on GPR signals [12,13]. Theoretically, the technology should also be able to detect the roots of agronomic crops, and as such, GPR is attracting research interest in agriculture [14–17]. Within GPR studies, roots and the surrounding soil often compete for visibility on B-scans, with soils that are heavy in clay negatively affecting resolution and visibility both of roots and of other soil features [12]. As such, soils with low permittivity are preferred for root studies, as high permittivity can interfere with the detection of roots. Roots that absorb large amounts of water can affect the permittivity of the soil by drying it out, and thus making the soil less responsive to electric fields [18]. Roots, even those fine in scale, can affect overall soil permittivity due to their influence on overall soil moisture content. Even so, it is difficult to determine the extent to which this can happen in field settings due to the variety of other variables that influence electric permittivity, and conclusive results have only been achieved in highly controlled settings [19].

The antenna used in this study operates over the frequency range 0.9 GHz to 2.7 GHz. As a rule of thumb, a quarter of the electromagnetic wavelength ($\lambda/4$) in the subsurface medium is required to determine the smallest separation necessary to distinguish between two nearby objects [20]. The minimum separation, or so-called “detection threshold”, varies depending on the velocity of the signal in the medium, and in an agricultural context, it is largely determined by field moisture levels. Using a range of values typically found in non-conducting materials of agricultural soil (commonly between two and ten), velocities of 0.21 m/ns to 0.09 m/ns, respectively, can be calculated using the equation:

$$v = \frac{c}{\sqrt{\epsilon_r}} \quad (1)$$

where c is the speed of light in a vacuum and ϵ_r is the relative dielectric (non-conductive) permittivity, or dielectric constant, of the soil medium [21]. In practice, this means that

the lowest frequency of the prototype antenna (0.9 GHz) used in this study corresponds to a detection threshold that ranges from 5.89 cm to 2.63 cm, while the highest frequency (2.7 GHz) corresponds to a detection threshold that ranges between 1.96 cm and 0.88 cm. As mentioned above, the images displayed in GPR scans represent reflection, diffraction, and backscatter of electromagnetic energy from objects buried in the subsurface. Visual representations of the reflected electromagnetic energy are typically viewed in one of two forms: an 'A-scan' is a single return which is displayed as a time-varying function with amplitude peaks and valleys on one axis and time on the other, and a 'B-scan', which is a pseudo-2D cross section of the subsurface formed when a series of A-scans is acquired along a survey path. In such a 2D radargram, the signal amplitude is often represented by brightness on a gray-scale, time is given on the vertical axis, and survey position is given on the horizontal axis. 'C-scans' further extend GPR data visualization by combining data from multiple B-scans to create a 3D data-cube. These have proven useful in projects attempting to map the subsurface in terms of depth as well as position relative to the visible x-y plane of the surface.

The depth potential of a GPR antenna depends primarily upon both its frequency and the quality of the soil on which it is being used. Frequency tends to be a trade-off in terms of resolution and penetration power: higher-frequency antennas (900 MHz to 2 GHz) have high resolution but relatively low ground penetration, while lower-frequency antennas (under 900 MHz) can penetrate several meters into the ground but provide low resolution. In the case of this study, a high-frequency antenna (0.9 GHz to 2.7) was used as the targets were close to the surface and required a higher resolution in order to distinguish between roots and undesirable underground features (lower frequency is more common for examining groundwater tables or piping).

Time analysis, as in many forms of remote sensing, is important in determining spatial relations for objects of interest, especially as it relates to depth. The amount of time it takes for the reflection of electromagnetic waves to travel from transmitter to target to receiver can be used to calculate the depth of the target given the velocity of the signal in the soil medium. This, combined with the dielectric properties of the targets and soil media, begins to paint a picture of the structure of the subsurface, which can then be used to distinguish the targets from their surroundings.

The application of GPR is an approach that is being successfully tested as a tool for precision agriculture [17]. The present study assesses the feasibility of root biomass quantification by exploring correlations between features extracted from GPR responses and harvested belowground biomass. Root detection by GPR shows promise for further development both in theory—since roots present a dielectric contrast to the host soil—and based on previous studies documented in the literature [14–16,22]. Most of these studies have adopted an image analysis approach to quantify the presence of belowground biomass. For example, radargram pixel counts have been used to quantify the mass of cassava tubers [14]. A similar pixel-level image analysis was used to predict peanut yield [15]. An alternative to an image analysis approach is a frequency-based analysis where the GPR signal is decomposed into its component frequencies, which are then evaluated as features predictive of biomass. Observed root biomass of cassava and peanut has been predicted using this method [16,23]. An additional alternative for GPR feature extraction is the use of wavelet methodologies. Wavelet analysis in GPR has been largely applied as a de-noising technique [24,25]; wavelets have also been applied in a diagnostic capacity in civil engineering [26] as well as in evaluation of soil moisture [27]. The fibrous and rhizomatous biomass assessed in this current study are characterized by a lack of a single large, discrete target object and are distributed among three depth layers. The dispersed nature of both the biomass and the signal makes a wavelet-based time/frequency analysis more appropriate in this case.

The objective of this study is to determine the ability of the continuous wavelet transform (CWT) technique to identify and quantify the belowground material of a perennial sorghum hybrid based on GPR B-scans. We hypothesize that correlations between B-scan

wavelet pseudo-frequencies (WPFs) features and dry biomass will produce an accurate representation of subterranean sorghum that can be used as a proxy for belowground mass measurements in the field. The relevance of this correlation is that greater biomass in root structures is indicative of greater carbon sequestration, making GPR an appropriate tool to assess carbon sequestration potential in agricultural ecosystems defined by perennial grasses.

2. Materials and Methods

To test the working hypothesis that belowground root and rhizome biomass is detectable via GPR using a time-frequency analysis hypothesis, a sorghum hybrid selected for high belowground biomass was grown as a monoculture in a pure sand environment. The root and rhizome systems were scanned using a prototype GPR antenna, and then harvested biomass information was regressed against features extracted from the radargrams. Signal features were derived using time-frequency analysis on B-scans via the continuous wavelet transform (CWT). A high-level process overview is given in Figure 1.

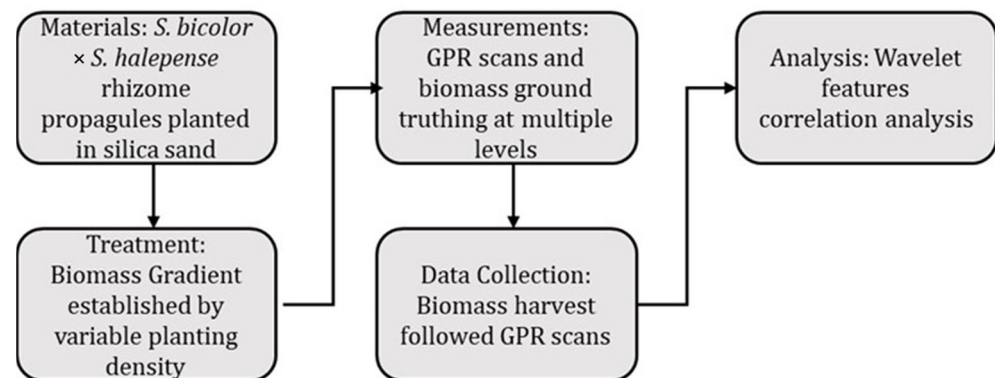


Figure 1. High-level flowchart of study design.

The sorghum hybrid *Sorghum bicolor* L. Moench × *Sorghum halepense* L. Pers (i.e., PSH09TX15) used for this study was kindly provided by Dr. Russell Jessup (Texas A&M, College Station, TX, USA) [28]. This hybrid is generally sterile and grows to a height of ~2 m. It was chosen due to its dense rooting growth characteristic and method of propagation via rhizomes, which are produced with a diameter of ~1 cm and serve as the emanation point of the plant's fibrous root system [28]. Rhizomes comprise modified stem tissue that grows laterally beneath the soil's surface to produce new clone shoots from their nodes. They can persist from season to season, and have been shown to accumulate mass over multiple growing seasons [29]. Additionally, rhizomes have the capability of growing with a smaller energy investment in each subsequent growing season. This capability results in a crop that can sequester carbon more effectively than an annual crop.

The aboveground planted PSH09TX1 material was mowed to the soil media surface, and the troughs scanned with a prototype air-launched GPR antenna array developed by IDS GeoRadar (Golden, CO, USA). The latter utilizes a unique air-launched resistively loaded vee dipole antenna design, which had been developed as a means to detect buried objects without the necessity of ground contact [30–32]. The antenna array unit has been used in other published research [15,16,23,33] and is pictured in Figure 2. An air-launched antenna was used because of its greater suitability for scanning uneven agricultural surfaces with the accepted trade-offs of a strong ground return and less energy being transmitted into the soil subsurface than with a ground-coupled unit [34]. The antenna array used was mounted onto a cart at a height of approximately 50 cm from the soil's surface (Figure 2). This height was chosen to prevent the overlap of the direct wave and the surface return [34]. The antenna was oriented in a direction normal to the soil's surface to minimize the amount of energy reflected away from the subsurface. Plants were scanned only in the long-direction with respect to the trough due to the narrow trough width. An encoder wheel

was mounted to the base of the cart and was used to gather one A-scan every centimeter traveled, as seen in Figure 2. While an exact GPR footprint is difficult to determine, communications with the manufacturer of the antenna estimated that the expected “view” of the antenna was approximately elliptical, with a 60° swath in the front-to-back look direction and a 120° swath in the left–right direction, corresponding to an ellipsoid with a short-axis of approximately 114 cm and a long-axis of approximately 200 cm at a height of 50 cm. A-scan returns were gathered along the path of travel at a regular interval of 1 return per centimeter using an attached encoder wheel. In the context of this study, A-scans were averaged into observations based on which plot they were collected within; the smallest of which was 117 cm long, which corresponded to 117 returns.



Figure 2. Photograph of data collection using IDS antenna array. Antenna was mounted on an aluminum cart and moved from one end of the trough to the other during data collection.

Experimental plots of PSH09TX15 were established from rhizome propagules. The plots were located at the Texas A&M University Farm (30.530, -96.426) and consisted of an aboveground trough constructed with a post-and-rope structure supporting an enclosed growth matrix lined within a weed cloth barrier (Figure 3b). The trough was filled with 100% silica sand. The artificial environment pictured, referred herein as a ‘trough’, was divided into individual plots with boundaries defined by the posts making up the wall. The target plots and buffer plots on each end had an average length of 2.6 m, width of 2.1 m, and depth of 1.1 m. Prior to filling the troughs with the sand, nylon nets were installed at three different depths. The nets were used during harvest to separate belowground biomass into different layers following the removal of growth substrate. A top view and a side view of the trough setup is shown in Figure 3a. Plants were irrigated via a drip tape and fertigated as needed via liquid fertilizer injector.

After the GPR scanning, the weed cloth barrier supporting the sides of the berm (shown in Figure 3c) was removed, exposing the bare sand matrix. The troughs were washed with a high-pressure water hose over the course of one week, resulting in the gradual exposure of root material (see Figure 3b). The fibrous root systems and rhizomes were captured by the nylon nets in the three different accessible layers. Measured from the soil’s surface, the thicknesses of each of the layers were 15, 45, and 45 cm (see side view in Figure 3a). The fibrous roots and rhizomes were then harvested by hand. Plant crowns were included in the collected tissue of the top zone, and were separated into tissue groupings of either fibrous roots or rhizomes depending on morphology. Roots were severed where they crossed the nylon nets that separated adjacent layers. Roots were collected within each plot (see top view in Figure 3a) at each of the three layers. Harvesting

took place immediately after the washing process had concluded, and the root material was dried in a greenhouse in order to preserve mass against microbial degradation. The root samples were then re-washed in large plastic containers to remove excess sand. During the entirety of the washing process, care was taken to retain rhizome tissue and the fibrous root system (i.e., roots with an approximate diameter of ~1 to 4 mm). However, the fibrous system was not further separated into size-based subcategories due to the lack of resources to process the amount of material. All plant material examined in this study, therefore, is either the rhizome tissue, the fibrous root tissue, or the sum of these two groupings. Samples were hand-separated into two main tissue sub-groups: rhizomatous and fibrous root biomass. Each sample was then dried in an oven at 60 °C until its weight stabilized to remove variability in measured mass due to water content.

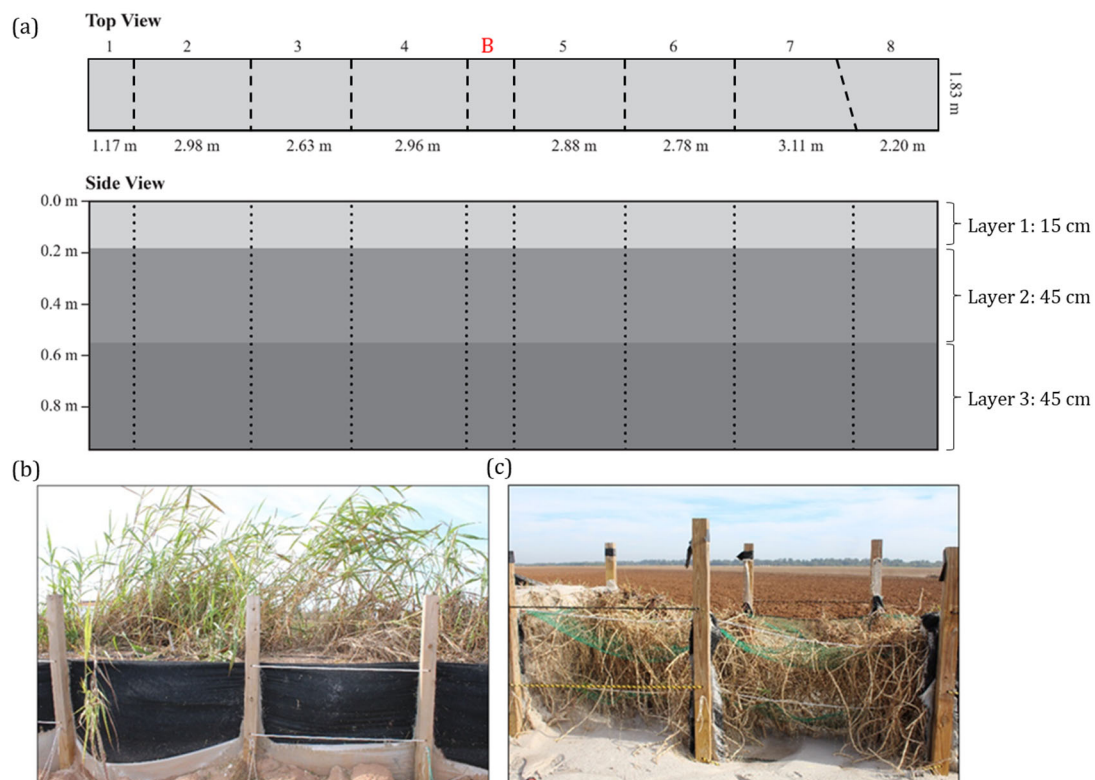


Figure 3. Descriptive images of trough system. (a) From left to right, plots are numbered 1–8 (see top view). The space labeled ‘B’ was intended as a blank area and no associated mass was harvested. The different layers are demarcated with different shades of gray. (b) Artificial trough environment during growing season. (c) Belowground biomass following trough washing process. Pictured are the three depth layers separated by the green nylon netting.

The GPR workflow (Figure 4) comprises a small number of key steps. The processing and analysis was performed using GPR-Studio version 1.0.1 (Crop Phenomics, College Station, TX, USA, (cropphenomics.com, accessed on 14 June 2023)), an in-house software combination of graphical user interface and Python library that provides GPR processing, analysis, and visualization services. A notable difference between the data in this analysis and that from other surveys is the lack of distinct visual features in the raw radargrams. In many other contexts, GPR data produces characteristic hyperbola features present prior to any preprocessing steps that are taken. The data examined in this study had no similar obvious features that could be directly attributed to plant mass. As such, part of our working hypothesis is that any detection is of bulk material as opposed to individual roots or rhizomes. This is not to say that the current method is not applicable to the detection of individual fine roots, however, but that specific application is not explored in the current study. While performing the exploratory analysis of B-scans, it was found that GPR

processing workflows involving certain widely applied signal-processing techniques (e.g., bandpass filters, gain correction) produced inconsistent results. With regards to bandpass filters, at this stage in the field's development, it is uncertain which frequency ranges correspond to noise and which ranges indicate the presence of target biomass. The net result of any filtering operation is always the removal, or at least the alteration, of potentially informative features. Generally, it is wise to proceed only with the simplest processing steps with the intention of addressing a particular aspect of the data [35]. With this in mind, the final preprocessing workflow used was a minimal pipeline, illustrated below.

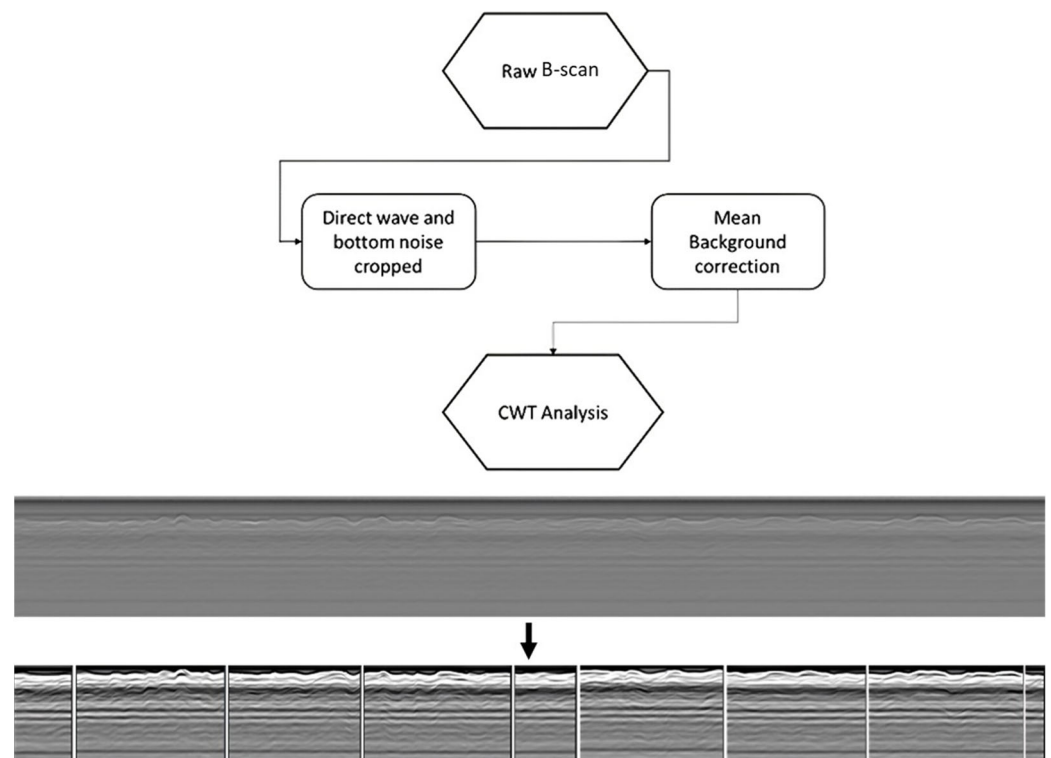


Figure 4. Processing flowchart and visual result. Chart shows the pre-processing steps used to prepare GPR data for CWT analysis. Pictured above is the ‘before’ and ‘after’ representation of the GPR data used in this study. The ‘after’ depiction is the appearance of the data after ‘Cropping’ and ‘Background Correction’ steps prior to the use of the CWT.

The initial GPR processing step is the cropping of the B-scan to remove regions known to contain unwanted non-informative signals. The raw B-scan is cropped to exclude the direct wave and associated ground clutter (normally indicated by the high-amplitude bands at the top of the section), as well as any samples recorded after 32 ns two-way travel time. The latter region appears to contain mostly deeper soil horizons beneath the trough system and/or multiple reflections of a shallower structure. Multiples may be generated as a direct result of the engineering of the prototype antenna hardware (verbal comm., A. Delgado, IDS GeoRadar, 2018, Pisa, Italy). The appearance of strong multiples in the GPR data was not anticipated prior to acquisition.

After cropping the radargram, background correction was performed. The background correction algorithm used in this analysis first computes the mean signal amplitude across each row of a given B-scan. The row-wise means are then subtracted from the B-scan. The expected result of this operation is the reduction of noise in the form of sub-horizontal bands of enhanced signal amplitude. These high-amplitude horizontal bands distort the desired information that is directly related to the compact three-dimensional root system.

The continuous wavelet transform (CWT) is a technique that localizes the individual frequency components contained within a time-varying signal. In GPR research, wavelets are often applied to analyze the response of topography [36] to detect objects such as

landmines [37] and to filter signals [38]. Wavelet application in agricultural root detection is based on the supposition that, similarly to spectrophotometry performed in a wet lab, distinct root sizes or structures will preferentially respond to specific frequencies in the electromagnetic wave. While similar to Fourier analysis, wavelet analysis has the key difference of identifying the signal frequency of interest in time, in addition to reporting the relative amplitude of each frequency. The recording of such frequencies of interest is performed by collecting scaled and translated versions of a ‘mother’ wavelet function across the extent of a mapped signal. The collection of the signal with the variously scaled and translated ‘daughter’ wavelets records the relative amplitude of a specific ‘pseudo-frequency’ (hereinafter referred to as a ‘wavelet pseudo-frequency’, WPF) at each instant of time within the signal. It is hypothesized that the presence of root mass can be predicted by analyzing the cohesiveness of all WPF components extracted from GPR B-scans of agricultural fields.

A novel application of CWT was used herein, similar to the one used in a prior analysis of electromagnetic induction survey data [39]. The observed biomass from the harvest was correlated with sums of the wavelet coefficients at a given WPF. The mother wavelet chosen for analysis was the complex Morlet wavelet [39–41]. The result of combining the complex Morlet wavelet with the GPR trace is a complex signal. We took into consideration only the size of the resulting wavelet coefficients, which is obtained by computing the vector length of a given sample. These size values are then summed within an agricultural plot to produce a GPR feature that corresponds to a given biomass measurement. The complex Morlet wavelet was chosen because it resembles the emitted GPR pulse, with the idea that reflected pulses, though distorted and attenuated by the propagation through the soil medium, would retain the basic frequency content of the emitted pulse. Each sum was divided by the length of its respective plot. The feature investigated here is thus coined a ‘wavelet pseudo frequency density’ (WPDF) measure. The biomass measurements were also divided by the length of their respective plots. This division was performed to standardize both WPF feature and biomass values because the sizes of the trough plots varied (the smallest plot was 1.17 m in length, while the longest was 3.11 m). The standardization was performed to make the data values between each of the differently sized plots comparable.

Biomass values collected for each layer were compared using an ANOVA test to demonstrate existing variability at different depths ($N = 27$). Following this ANOVA, a Tukey’s HSD post hoc test was performed to determine which layers differed from each other. The results of both tests can be found in the Appendix A. These tests were both performed in R studio. For each tissue grouping at each depth layer, an experiment was conducted wherein the Pearson correlation coefficients (R statistics) were calculated at each WPF using the open source ‘scipy’ Python library ($n = 8$ for each layer) [42]. These correlations were evaluated based on their corresponding two-tailed p-value. After calculating the correlations, each WPF was evaluated for the strength of its relationship with belowground mass. The strongest of these correlations for each experiment was reported, and the strongest of this subset were further analyzed by generating a simple linear regression equation describing the line of best fit between the WPFs and the standardized mass values. These correlations were further analyzed using a bootstrapping analysis with 1000 iterations implemented with the open source ‘numpy’ Python library to comment on the robustness of each statistic and the associated regression equation.

3. Results

3.1. Belowground Biomass Analysis

It is evident that the variance in the rhizome mass was much higher than that of the fibrous roots within each of the three layers (Figure 5). Notably, about 85% of the total collected material was composed of the comparatively persistent rhizome tissue.

The results of the ANOVA test (Table 1) demonstrate that significant differences in belowground biomass variability exist between the layers and between belowground tissue types (fibrous roots and rhizomes). The results of the Tukey’s HSD post hoc test (Table A1)

show that belowground tissue type differences are significant ($p < 0.0001$). Significant differences were also found between the top and middle ($p < 0.01$) and the top and bottom ($p < 0.05$) depth layers. No significant difference ($p > 0.05$) in mean root-mass was found between the middle and bottom depth layers. These results for the Tukey's HSD can be found in Appendix A. The greatest rhizome mass was found at layers 2 and 3 (See Figure 6). A similar trend is followed by the fibrous roots, though to a lesser extent. Likewise reflected in the harvested biomasses is the lower mass values of the first and last plots caused by variable planting density used in this study to derive the GPR root and rhizome mensuration algorithm.

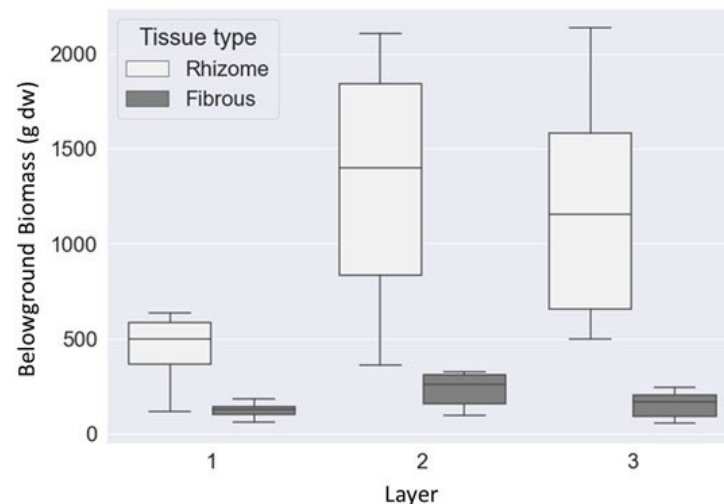


Figure 5. Box and whisker graphs of root and rhizome tissue biomass per layer. Distributions of both tissue types are shown in three sets of two graphs, with each box and whisker corresponding to the mass measurement distributions for a given layer across all eight agricultural plots for one of the two tissue types.

Table 1. Summary of ANOVA evaluating variability between layer and biomass tissue type. Differences were detected within both variables to a significant degree.

	DF	SS	MSE	F	Pr > F	
Layer	2	2,127,394	1,063,697	6.387	0.00367	**
Tissue	1	8,074,213	8,074,213	48.48	1.30×10^{-8}	**
Residuals	44	7,328,131	166,548			

** $p < 0.01$.

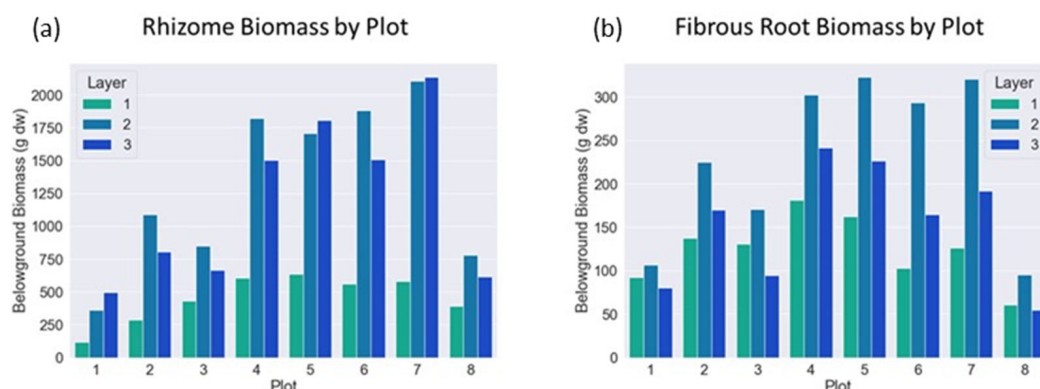


Figure 6. Biomass distribution. Bar graphs of biomass measurements per layer for each agricultural plot demonstrate hybrid's propensity for deep deposition of recalcitrant mass. (a) Mass measurements of rhizomes. (b) Mass measurements of the fibrous root samples.

3.2. Time Frequency Analysis

The result of the CWT analysis on a given B-scan is a cube wherein each ‘slice’ of the cube’s third dimension is visualized as an image whose pixels represent the fit of a daughter wavelet of a given scale to the original signal at that location. Each of these images corresponds to a different WPF (this concept is illustrated in Figure 7a). To obtain the Pearson correlation statistic, r , the real part of the pixel values within each WPF image were first summed. This sum, as well as the biomass measurement, was then divided by the length of its respective plot to obtain a normalized WPDF measure and biomass measurement. These two features were then correlated with each other to determine the connection between belowground biomass and the GPR feature. Each mass type and depth range evaluated can essentially be thought of as its own experiment (for example, the correlation of radar features and fibrous root mass at the top depth herein is viewed as a separate experiment from rhizomes at the top depth). Each of these experiments had a sample size of $n = 8$, where each observation is the summary of signals within a given agricultural plot, as seen in Figure 3. The results of the CWT analysis are herein presented as line graphs of the R statistic as a function of WPF. The strongest correlations are shown both in Table 2 and in Figure 8.

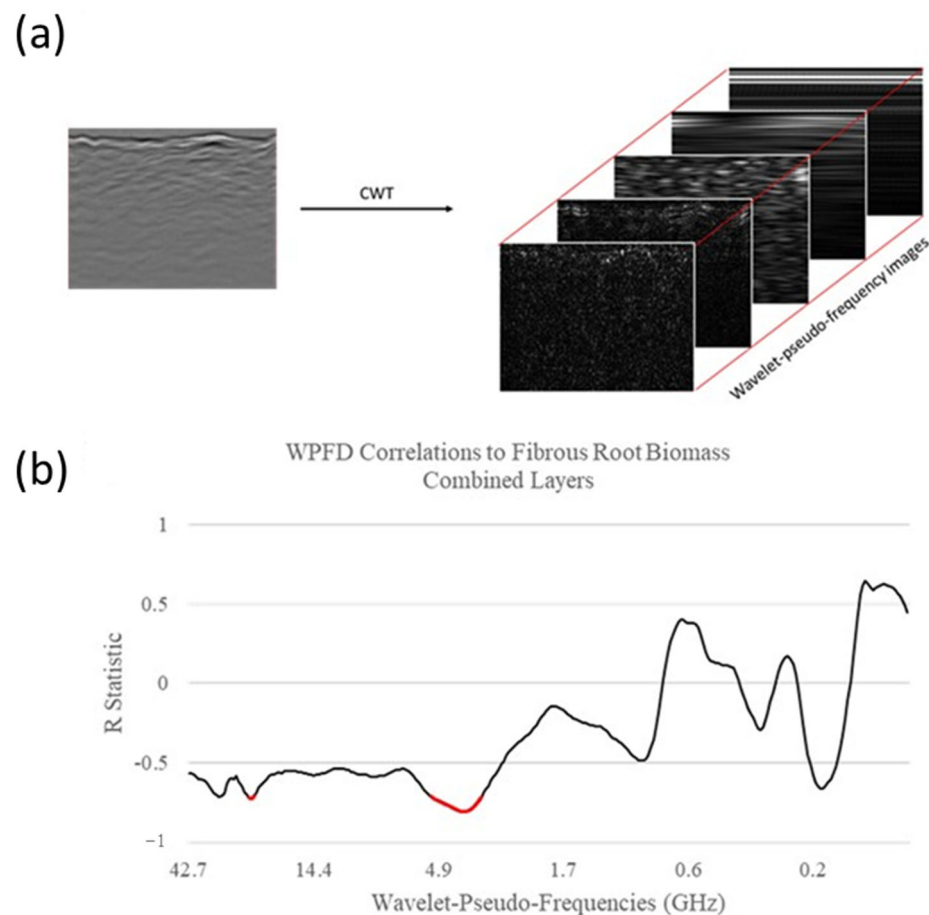


Figure 7. Analysis initial result. (a) Depiction of resulting data following CWT. (b) Sample graph showing the correlation of fibrous root mass values with WPDF features. Frequencies highlighted in red were found to be significant at $p < 0.05$ ($N = 8$).

Table 2. Highest WPF correlations. All results shown are the strongest correlation between biomass and WPF at each depth (layer) for each experiment. Experiments are designated by the layer(s) and tissue columns (note: “Combined” refers to summed fibrous and rhizome mass).

Frequency (GHz)	<i>p</i>	R	Tissue	Layer(s)
14.4	0.002	−0.91	Fibrous	1
0.4	0.021	−0.78	Rhizome	1
0.4	0.027	−0.76	Combined	1
3.9	0.014	−0.82	Fibrous	2
1.3	0.048	−0.71	Rhizome	2
0.2	0.055	0.70	Combined	2
2.8	0.138	−0.57	Fibrous	3
0.1	0.131	0.58	Rhizome	3
0.1	0.148	0.56	Combined	3
4.3	0.003	−0.89	Fibrous	1 and 2
3.1	0.060	−0.68	Rhizome	1 and 2
3.2	0.048	−0.71	Combined	1 and 2
3.9	0.016	−0.80	Fibrous	All
2.8	0.090	−0.63	Rhizome	All
2.9	0.080	−0.65	Combined	All

Each of the line graphs was produced by correlating the biomass measurements within a given set of layers with the WPF calculated from the same layers. For example, the graph shown in Figure 7b was generated by correlating the sum of fibrous root biomass across all three layers against WPF values derived from each of the WPF images, as per Figure 7a. These graphs were created to explore how well different WPF ranges correlated to belowground biomass. Figures A1 and A2 show these plots for all experimental combinations tested.

All of the WPF correlations were filtered by their *p*-value using a threshold of $p < 0.05$. The resulting peak WPF ranges are denoted on these line graphs by a red highlight (e.g., Figure 7b). Interestingly, all significant correlations generated from this analysis were negative; this is to say, a high WPF corresponded to an absence of belowground biomass (Table 2, Figure 7b at WPF ~5 GHz, Figures 8 and 9). None of the biomass groups (fibrous root, rhizome, or total biomass) correlated well with any WPF at layer 3. This suggests that signal fading may have resulted in a loss of necessary information to detect roots beyond an approximate 60 cm depth. Conversely, all biomass groups produced significant correlations to WPFs evaluated from the top 15 cm of data.

The fibrous root system and rhizomes correlated significantly to layer 2; however, the combined biomass did not. Because the first two layers correlated significantly to both fibrous roots and rhizomes, the masses of these two layers were pooled and correlated with the WPFs for this new region of interest. From this, only the total mass correlated significantly. Finally, all biomass groups were tested for correlation to WPFs calculated for all three layers. From this, only the fibrous root system correlated significantly to any of the WPFs for total biomass in layer 3. When examining the line graphs in Appendix A, rhizomes appear to correlate well at WPF ranges lower than 2 GHz, whereas fibrous roots peak close to 4.9 GHz at both layer 1 and layer 2. The chart depicting the total biomass evaluated at layer 1 appears to peak in ranges similar to both rhizomes and fibrous roots; however, evaluation at layers 2 and 3 shows a peak similar only to the fibrous root system.

The further analysis of the highest-performing WPF features yielded simple linear regression equations that differed in both their slope and intercept. Both the intercepts and slopes appear to generally become steeper when considering increasing depth layers, which is likely related to a larger variation in the amount of biomass harvested (see Figure 5). The amount of variation explained by the dependent variable in all cases was greater than $R^2 = 0.50$, indicating that the chosen GPR WPF explains greater than half of the variation seen in the standardized biomass and thus appears to have predictive capability.

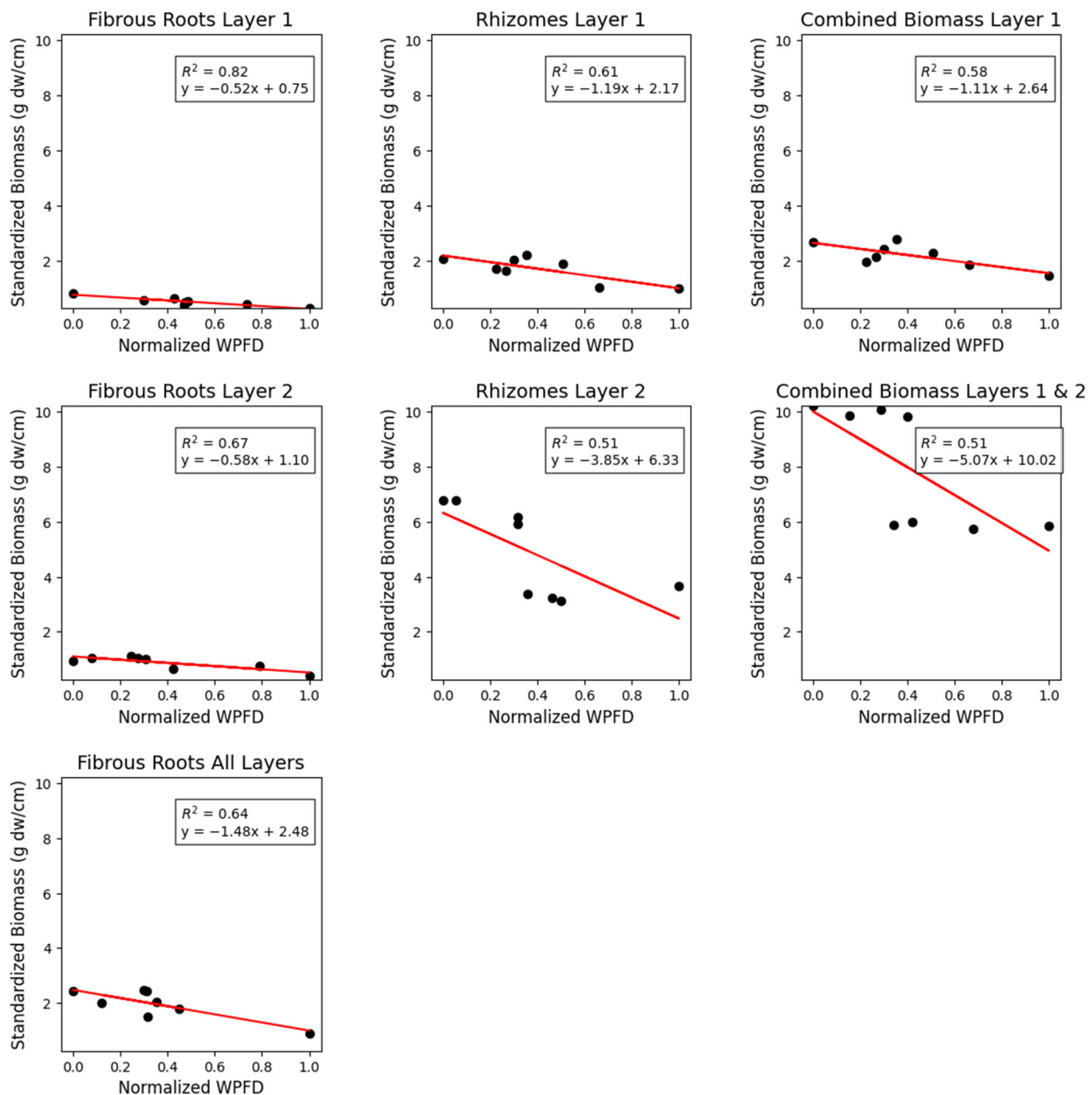


Figure 8. Scatterplots of highest-performing WPFs. Red lines shown are the least-squares line of best fit. Neither fibrous roots nor rhizomes correlated significantly with any WPFD feature at layer 3. All correlations shown are significant to $p < 0.05$ ($n = 8$).

To test the hypothesis that the variation between the different regression equations was mainly due to mass, the standardized biomass measurement shown in Figure 8 was further transformed via normalization, such that the maximum and minimum measurements for each experiment were 1 and 0, respectively. After this transformation (Figure 9), the differences in slope and intercept are much less apparent between depth layers and tissue type. The main differences at this point are simply the strengths of each relationship, as indicated by R^2 .

The validity of the R-values were further evaluated by utilizing bootstrapping wherein each tissue group \times depth layer combination was resampled with replacement over the course of 1000 iterations, and the correlation statistic recalculated. Histograms representing the results of this analysis are shown in Figure 10. Mean R-values obtained from this process are shown in Table 3, along with the observed R values from Table 2. All mean R values were close to the observed values. Further, four of the seven reported correlations

have 95% confidence intervals with bounds well away from 0, suggesting that even if the actual correlation is different from the mean, it is highly likely that there is at least some correlation between selected GPR features and biomass.

Table 3. Mean R and confidence intervals for bootstrapping of selected correlations.

Tissue	Layer (s)	Observed R	Mean Bootstrapped R	95% Confidence Interval
Fibrous	1	−0.91	−0.87	[−0.99, −0.52]
Rhizome	1	−0.78	−0.71	[−0.96, 0.19]
Combined	1	−0.76	−0.69	[−0.97, 0.01]
Fibrous	2	−0.82	−0.76	[−0.97, −0.26]
Rhizome	2	−0.71	−0.74	[−0.99, −0.38]
Combined	1 and 2	−0.71	−0.71	[−0.94, −0.37]
Fibrous	All	−0.80	−0.70	[−0.97, −0.04]

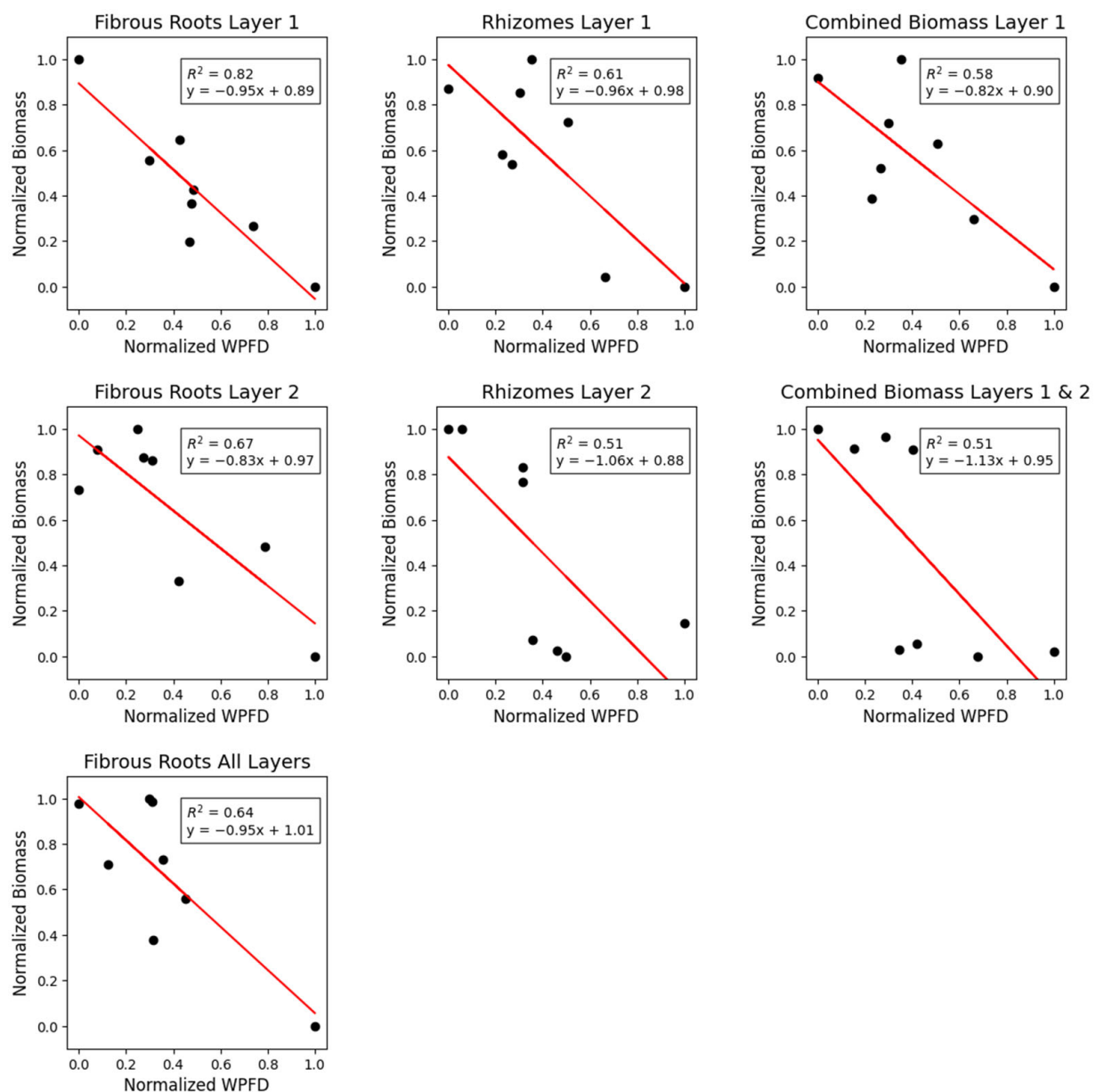


Figure 9. Scatterplots of highest-performing WPFs with normalized biomass axes. Red lines shown are the least-squares line of best fit. Data for each experiment were transformed so that all biomass measurements varied between bounds of 0 and 1 to eliminate differences in apparent regression equations due purely to mass.

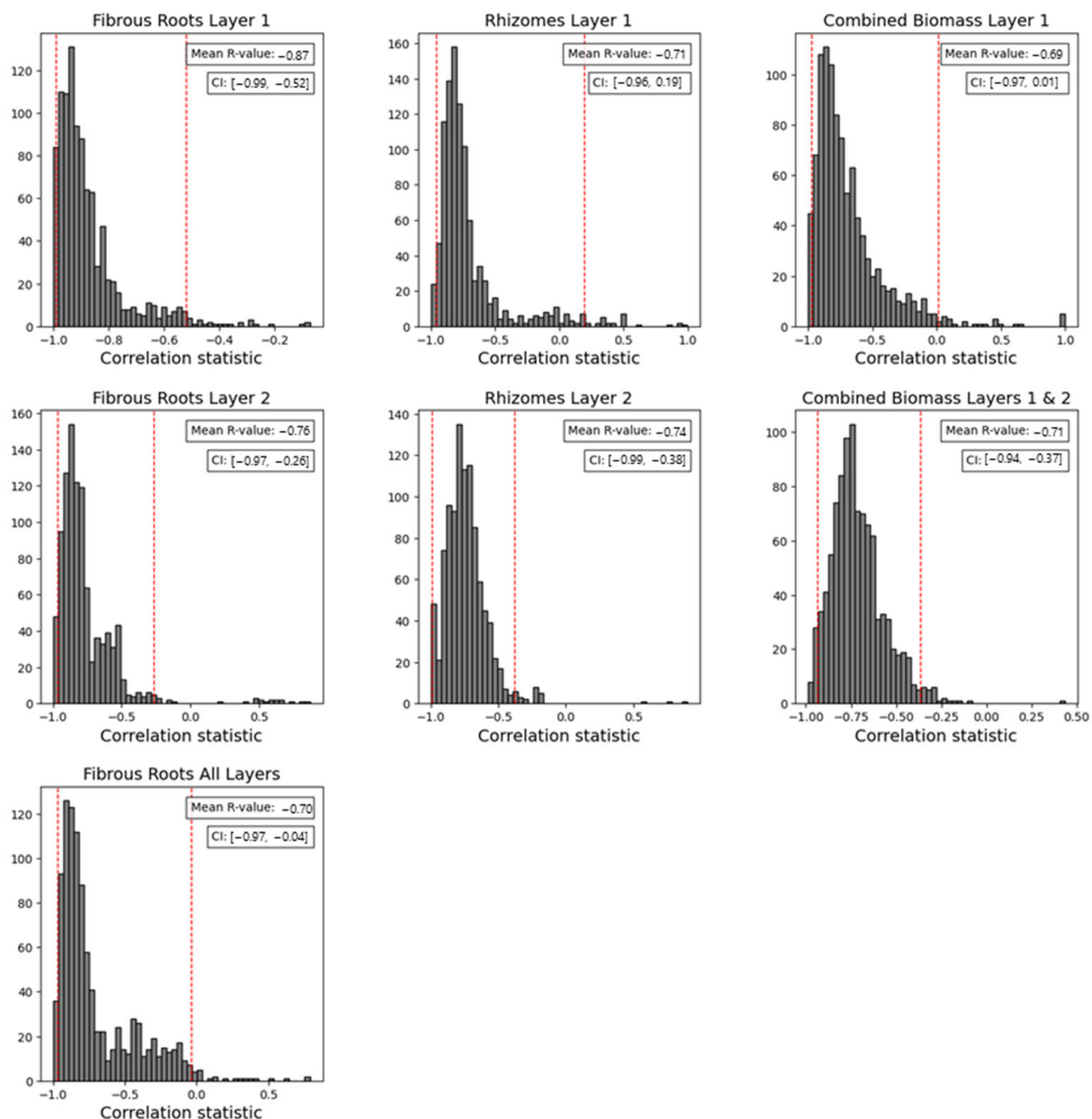


Figure 10. Results of bootstrapping analysis on highest-performing GPR features. All features plotted in Figure 8 underwent bootstrapping using 1000 iterations. Resulting mean R-values and confidence intervals are shown here as well as in Table 3.

4. Discussion

The wavelet analysis produced significant correlations at several distinct WPFs, depending on the layer and tissue type of the biomass. Most interestingly, all significant correlations found in this work indicate a negative relationship between biomass and the wavelet feature.

The bootstrapping analysis showed that after 1000 iterations, the derived mean correlation statistics were close to what was observed in the original experiments. The 95% confidence intervals further confirmed the existence of relationships for the fibrous root system at layers 1, 2, and all layers combined; rhizomes at layer 2; and the combined biomass in the combined top two layers. The results of this analysis are encouraging, as they further validate the observed statistics shown in Table 2. However, it is also worth noting that the histograms shown in Figure 10 demonstrate that while it is likely that the correlations exist, they may be substantially weaker than what is observed.

The regression equations defining the lines of best fit for the observed relationships differed in their y-intercept values and slopes. This was shown to be due to the differences in the amount of mass being considered for each separate experiment. As greater depths contain more variation in biomass and the x -axis will always be between 0 and 1, an increase in slope and intercept are to be expected. It should also be noted that this observation regarding these equations can only be inferred from the experiments examining the fibrous root system and the experiments examining rhizomes at the top two layers, as the other experiments detailed here investigated various combinations of mass and depth layers.

Negative relationships between belowground biomass and GPR signal features have been reported in the previous literature [43], and correlations have been shown to switch from negative to positive at progressive depths [15]. A possible explanation for negative relationships is that the presence of a root zone may result in less soil compaction, thus causing a weaker reflection at the surface. Another possibility is that PSH12TX09's complicated root architecture results in an attenuation of certain frequencies resulting in a detection method analogous to absorbance techniques used in wet labs. An important takeaway from the plots of correlation vs. WPF (Figures 7b, A1 and A2) is that there are ranges within which biomass correlates well to the GPR signal. This could potentially be leveraged in future studies by effectively using CWT analysis as a filter to remove information outside of a given WPF range.

Belowground plant structures in this study were sub-classified as fibrous root or rhizomatous tissue, a helpful distinction in the exploration of detectability with ground-penetrating radar. A majority of the PSH12TX09 hybrid's belowground biomass is contained in the rhizome tissue. This finding has positive implications for the use of rhizomatous plants as carbon sequestration targets, as perennial rhizomatous crops can survive between seasons. This, in turn, encourages no-till agricultural practices and provides a system that can continually deposit root exudates without requiring the re-investment of energy for a new growth cycle. Contrary to expectations, the fibrous root system, despite making up a minority of the total biomass, had stronger correlations and wider significant WPF ranges than the rhizome root system. This may be due to different interactions of the GPR signal and growth environment to the fibrous root system as compared to their interaction with the system of rhizome tissue. A second possible explanation is that the correlation at low frequencies is the result of a strong association between the vascularly connected belowground fibrous root biomass and the near-surface crown structures. During the harvesting and classification of biomass, no effort was made to determine whether fibrous roots originated from the crown or from rhizome tissue. Given the presence of crown material during scanning (see Figure 3c for visual reference of crown size), returns associated with the belowground fibrous root system crown structure could be co-correlated with crown mass.

As the frequency of a GPR signal return corresponding to a large object would typically be low, the expectation is that belowground tissue with a larger radius would be correlated with lower wavelet frequency. In general, this was consistent with this study's results; however, the fibrous root system exhibited significant correlations at lower frequencies in addition to higher frequencies (see Appendix A). This was unexpected. However, a possible explanation warranting further study is that individual fibrous roots do not solely interact with EM radiation in the expected higher frequency ranges but are also detected as an 'aggregate root zone'. This hypothesis is partially supported by the results shown in Appendix A, as fibrous roots correlate with multiple WPF ranges. Moreover, the resolution limit for detection using radar can be estimated using the $\lambda/4$ rule of thumb [20]. With the current instrument's frequency range of 0.9–2.7 GHz, this limit prevents resolution of objects less than ~0.88 cm in length. This is much larger than a typical diameter of fine roots or root hairs but potentially of the same scale as rhizomes and the spatial changes in root architecture and/or the root system's zone of influence (i.e., the area within which water interacts with the root system). Alternatively, the correlation to the lower frequencies may be due to these frequencies responding to the near-surface crown structure that derives

the plant stems and large network of vascularly connected fibrous roots. This fraction of the fibrous root system was quite large, yet not segregated from the lower biomass of fibrous roots originating from the rhizome nodes. Collectively, the relatively large size of the entire root system and its zone of influence is a positive indicator for detectability and belowground mass quantification.

There is limited consistency with which WPFs correlate strongly with biomass as burial depth increases. The lack of a clear relationship between WPF and biomass at each burial depth suggests that morphological structures may respond differently at varying burial depths. The lack of a consistent radar signature using this approach could present a challenge moving forward, as the eventual goal for this technology is its application in realistic settings where soil conditions and root mass are not known beforehand.

The use of wavelet transforms in GPR biogeoscience research is relatively new. Wavelets were discussed in a review by Liu [38], who noted their use in various engineering applications, primarily as a de-noising and feature extraction technique. The analyses presented herein have adapted wavelets for B-scan feature extraction, thus building on the earlier work [39]. An encouraging feature of these results is that the correlations for layers 1 and 2 were significant for both the rhizomes and fibrous roots. This result indicates that even though signal attenuation occurred, it was still possible to detect the biomass to a depth of 60 cm, a result that is highly encouraging for further applications of this technology in a field setting.

Despite these results, there are several additional factors that either affect the reliability of the results or the ability to apply GPR and CWT in other environments. The biomass of the root system may have been influenced by the soil quality used in the experiment. Sand was used for this study as it would have provided the purest soil medium and also would allow for cleaner root samples after washing. However, it is not typically grown in 100% pure sand, and as such, the vegetation material used in this study was subject to higher draining and less water content than usual. It was also uncharacteristically dependent upon fertilizers, which may have affected how much biomass accumulated in different soil layers. In this way, the GPR may have been biased toward the layers most affected by fertilization. There were also many opportunities for fibrous root material to be lost between scanning time and harvest. The roots were washed away over a period of a week, allowing ample opportunity to lose finer root mass due to the washing process.

The degree to which the soil medium composition and its moisture content affect the results was not explored in the present study; however, these variables are crucial to consider in GPR applications. The main strategy undertaken by using pure sand was to eliminate potential variation caused by more naturalistic soil media in order to maximize the chances for root detection. The expected behavior of repeated measurements in a more water-saturated and clay-like soil setting would be a more rapid attenuation of signal strength as it travels further into the subsurface [12]. Furthermore, the drying of soil media due to drainage would likely cause scans of the same area to appear substantially different, and some form of compensation would need to be used to control this effect. From another perspective, the strategic use of soil moisture may, in fact, be a tool that can be used to increase the efficacy of this detection technique at shallower depths in a manner similar to Liu et al. [43]. This being the case, this analysis methodology cannot be deployed in a practical sense without further research into its stability in other environments.

Although sorghum has previously been investigated using GPR [44], it differs from other crops with successful correlations due to its absence of tubers and relatively small root structures. While the presence of such structures may be more easily determined in a controlled environment (such as in a manicured sand trough), it will certainly be more difficult to differentiate between rhizomes and irrelevant materials (such as rocks or solidified soil) in a standard agricultural setting.

The sand troughs themselves may have presented some uncertainties for the data collected. Based upon their construction, it was nearly impossible to break the sample down into sub-samples without introducing measurement error to the harvest process. The

requirement to examine the roots in bulk thus limited the sample size and inhibited the ability to determine individual rhizomes.

While encouraging, it should be noted that the regression equations derived for each of the reported features cannot be directly applied to other settings. Foremost is the fact that each regression equation describes a standardized mass measure as a function of a standardized GPR feature. This standardization is itself specific to the dimensions of the experimental trough environment, which immediately makes applying the regression equations impossible for prediction in other settings. Second, the relationships found are based upon a small sample size which was demonstrated to influence the robustness of the results per the bootstrapping analysis. Third, these results are limited by the fact that they were obtained from a single experimental environment and a single plant model. It can be hypothesized that similar approaches may yield success when varying species and environmental factors given the essential physical principles the technique is based upon; however, this must be experimentally confirmed and validated. Regarding the application to other conditions, the current study serves as a starting point for this method by providing a set of relationships to be further explored, improved, and integrated into predictive algorithms.

5. Conclusions

The results show that GPR-based proximal sensing of belowground biomass of the target sorghum grasses is feasible using CWT-based time-frequency analysis. Belowground biomass correlated significantly up to $R = -0.91$, with GPR features extracted from wavelet analysis, thereby demonstrating potential predictive capability. Optimal results from the wavelet analysis are derived from the WPFs that maximally correlate with belowground biomass measures. However, there is a wider range of WPFs at which correlations with belowground biomass are statistically significant. Future work should focus on exploring how the information spanning a wide WPF range, which may represent the detection of rhizomes and roots in unique orientations, can be used to predict belowground biomass. Additionally, future studies should introduce soil conditions and different plant species as covariates to determine the degree to which this technique can be generalized as a measurement technique.

Author Contributions: Conceptualization, M.E.E., M.B., R.J. and D.B.H.; Data curation, M.W., I.D.D. and H.A.R.-G.; Formal analysis, M.W., I.D.D., D.H. and M.B.; Funding acquisition, M.E.E., M.B., R.J. and D.B.H.; Investigation, M.W., H.A.R.-G., B.L.T., T.A., R.J. and D.B.H.; Methodology, I.D.D., D.H., B.L.T., M.E.E., M.B., R.J. and D.B.H.; Project administration, D.B.H.; Software, I.D.D. and H.A.R.-G.; Supervision, D.B.H.; Visualization, I.D.D.; Writing—original draft, M.W.; Writing—review and editing, I.D.D., D.H., B.L.T., T.A., M.E.E. and D.B.H. All authors have read and agreed to the published version of the manuscript.

Funding: This work was supported with grants from the National Science Foundation award number 1543957—BREAD PHENO: High-Throughput Phenotyping Early Stage Root Bulking in Cassava using Ground-Penetrating Radar by Dirk B. Hays, and by the Department of Energy of the United States (ARPA-E Award, No. DE-AR0000662)—Development of ground-penetrating radar for enhanced root phenotyping and carbon sequestration, also by Dirk B. Hays.

Data Availability Statement: The data presented in this study are available upon request from the corresponding author. The data are not publicly available due to product commercialization.

Acknowledgments: The authors would like to thank the students at Texas A&M University who assisted with data collection in the field.

Conflicts of Interest: We, the authors of this paper, acknowledge a potential conflict of interest arising from our relationship with Crop Phenomics LLC. Coauthors D.B.H. and H.A.R.-G. hold positions as CEO and CTO, respectively, within the company that owns the software employed for a portion of the analysis presented in this study.

Appendix A

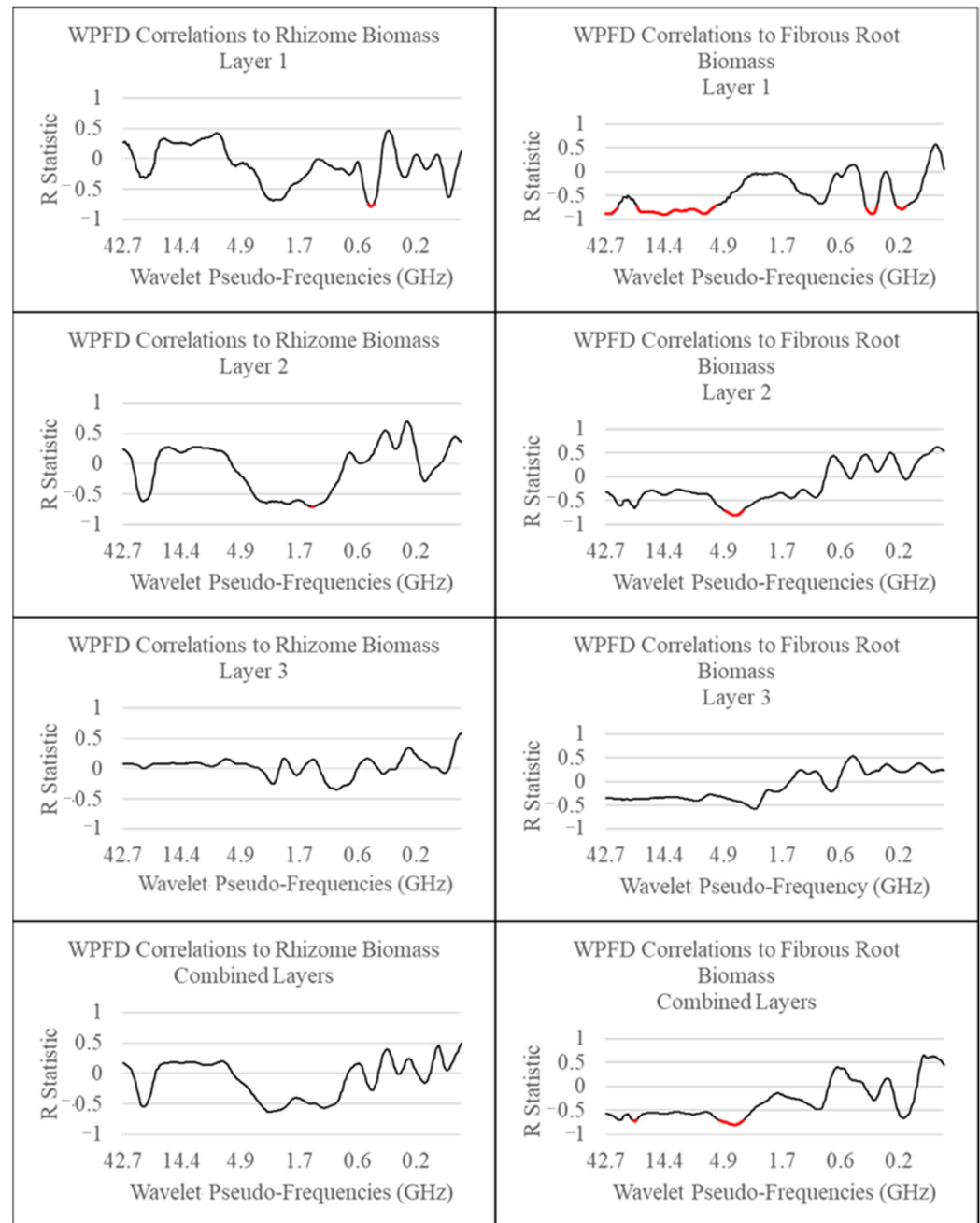


Figure A1. Plots of *R* statistic vs. WPF for each tissue sub-type. Shown are the full results for the multi-layer analysis. All portions of each graph that are highlighted in red represent WPFs that produced WPF features which correlated with biomass as an alpha of 0.05. Strongest correlations are reported in Table 2.

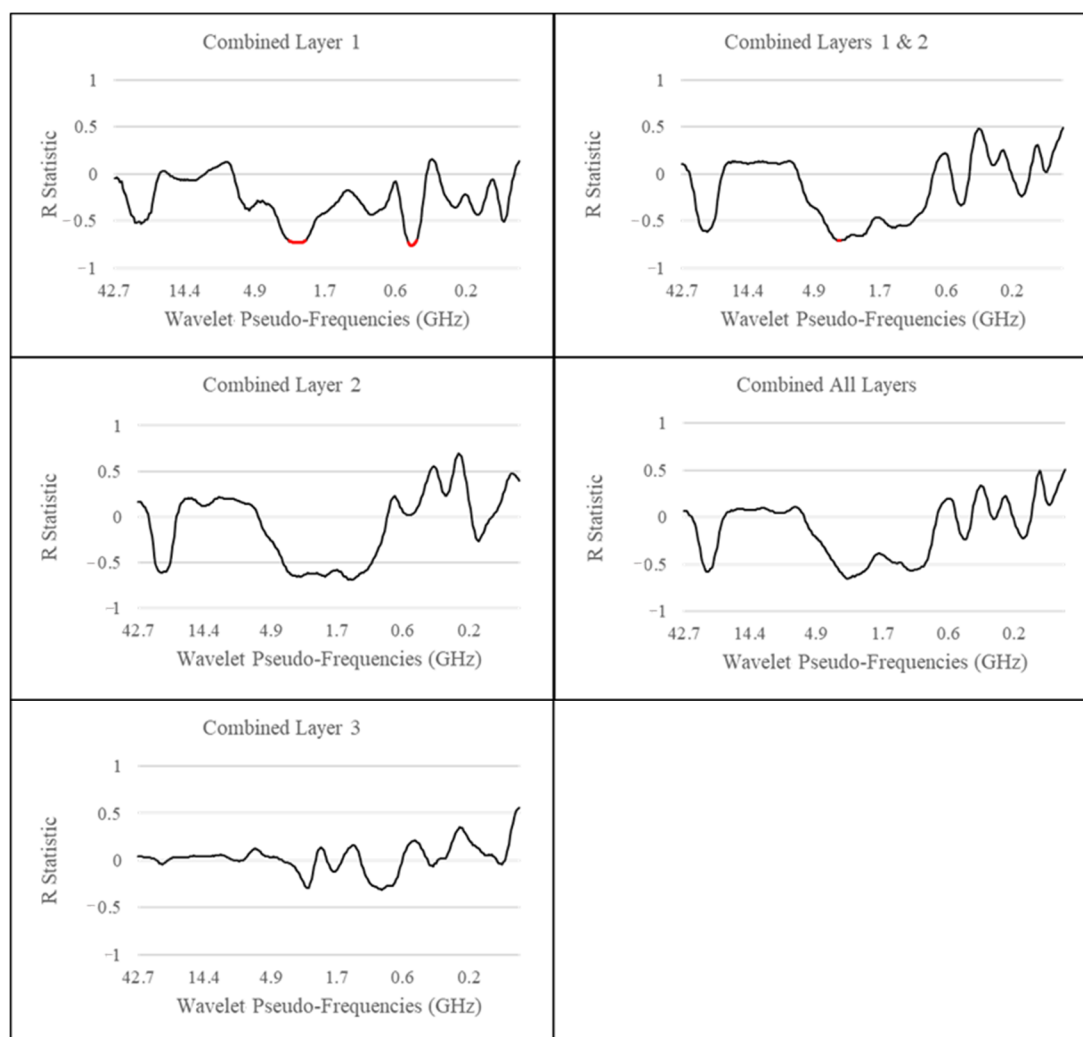


Figure A2. Plots of *R* statistic vs. WPF for total belowground biomass. Shown are the full results for the combined layer analysis. All portions of each graph that are highlighted in red represent WPFs that produced WPF features, which correlated with biomass as an alpha of 0.05. Strongest correlations are reported in Table 2.

Table A1. Tukey's HSD comparing biomass values between layers and between tissue types. 'R' and 'F' refer to rhizomes and fibrous root masses, respectively. Note, layers are numbered from top to bottom.

Tukey Multiple Comparisons of Means						
95% Family-Wise Confidence						
Fit: AOV (Formula = Mass ~ Layer + Tissue)						
p Adj	Upper		Lower	Difference		Layer
	0.004	839.74		139.81	489.78	2-1
	0.028	734.61		34.69	384.65	3-1
	0.748	244.84		−455.09	−105.13	3-2
p Adj	Upper		Lower	Difference		Tissue
	0	1057.7		582.85	820.28	R-F

References

- Allen, M.; Dube, O.P.; Solecki, W.; Aragón-Durand, F.; Cramer, W.; Humphreys, S.; Kainuma, M.; Kala, J.; Mahowald, N.; Mulugetta, Y.; et al. Framing and Context. In *Global Warming of 1.5 °C. An IPCC Special Report on the Impacts of Global Warming of 1.5 °C above Pre-Industrial Levels and Related Global Greenhouse Gas Emission Pathways, in the Context of Strengthening the Global Response to the Threat of Climate Change, Sustainable Development, and Efforts to Eradicate Poverty*; IPCC: Geneva, Switzerland, 2018.
- Schmidt, G.A.; Ruedy, R.A.; Miller, R.L.; Lacis, A.A. Attribution of the Present-Day Total Greenhouse Effect. *J. Geophys. Res.* **2010**, *115*, D20106. [\[CrossRef\]](#)
- Conant, R.T.; Paustian, K.; Elliott, E.T. Grassland management and conversion into grassland: Effects on soil carbon. *Ecol. Appl.* **2001**, *11*, 343–355. [\[CrossRef\]](#)
- Lemus, R.; Lal, R. Bioenergy Crops and Carbon Sequestration. *Crit. Rev. Plant Sci.* **2005**, *24*, 365–384. [\[CrossRef\]](#)
- Paez-Garcia, A.; Motes, C.; Scheible, W.-R.; Chen, R.; Blancaflor, E.; Monteros, M. Root Traits and Phenotyping Strategies for Plant Improvement. *Plants* **2015**, *4*, 334–355. [\[CrossRef\]](#)
- Lane, H.M.; Murray, S.C. High Throughput Can Produce Better Decisions than High Accuracy When Phenotyping Plant Populations. *Crop Sci.* **2021**, *61*, 3301–3313. [\[CrossRef\]](#)
- Zhang, J.; Lin, H.; Doolittle, J. Soil Layering and Preferential Flow Impacts on Seasonal Changes of GPR Signals in Two Contrasting Soils. *Geoderma* **2014**, *213*, 560–569. [\[CrossRef\]](#)
- Collins, M.E.; Doolittle, J.A.; Rourke, R.V. Mapping Depth to Bedrock on a Glaciated Landscape with Ground-Penetrating Radar. *Soil Sci. Soc. Am. J.* **1989**, *53*, 1806–1812. [\[CrossRef\]](#)
- Sucre, E.B.; Tuttle, J.W.; Fox, T.R. The Use of Ground-Penetrating Radar to Accurately Estimate Soil Depth in Rocky Forest Soils. *For. Sci.* **2011**, *57*, 59–66.
- Yoder, R.E.; Freeland, R.S.; Ammons, J.T.; Leonard, L.L. Mapping Agricultural Fields with GPR and EMI to Identify Offsite Movement of Agrochemicals. *J. Appl. Geophys.* **2001**, *47*, 251–259.
- Stokes, A.; Fourcaud, T.; Hruska, J.; Cermak, J.; Nadyezhdina, N.; Nadyezhdin, V.; Praus, L. An Evaluation of Different Methods to Investigate Root System Architecture of Urban Trees in Situ: I. Ground-Penetrating Radar. *J. Arboric.* **2002**, *28*, 2–10. [\[CrossRef\]](#)
- Butnor, J.R.; Doolittle, J.A.; Kress, L.; Cohen, S.; Johnsen, K.H. Use of Ground-Penetrating Radar to Study Tree Roots in the Southeastern United States. *Tree Physiol.* **2001**, *21*, 1269–1278. [\[CrossRef\]](#) [\[PubMed\]](#)
- Butnor, J.R.; Doolittle, J.A.; Johnsen, K.H.; Samuelson, L.; Stokes, T.; Kress, L. Utility of Ground-Penetrating Radar as a Root Biomass Survey Tool in Forest Systems. *Soil Sci. Soc. Am. J.* **2003**, *67*, 1607–1615. [\[CrossRef\]](#)
- Delgado, A.; Hays, D.B.; Bruton, R.K.; Ceballos, H.; Novo, A.; Boi, E.; Selvaraj, M.G. Ground Penetrating Radar: A Case Study for Estimating Root Bulking Rate in Cassava (*Manihot Esculenta* Crantz). *Plant Methods* **2017**, *13*, 65. [\[CrossRef\]](#) [\[PubMed\]](#)
- Dobreva, I.D.; Ruiz-Guzman, H.A.; Barrios-Perez, I.; Adams, T.; Teare, B.L.; Payton, P.; Everett, M.E.; Burow, M.D.; Hays, D.B. Thresholding Analysis and Feature Extraction from 3D Ground Penetrating Radar Data for Noninvasive Assessment of Peanut Yield. *Remote Sens.* **2021**, *13*, 1896. [\[CrossRef\]](#)
- Agbona, A.; Teare, B.; Ruiz-Guzman, H.; Dobreva, I.D.; Everett, M.E.; Adams, T.; Montesinos-Lopez, O.A.; Kulakow, P.A.; Hays, D.B. Prediction of Root Biomass in Cassava Based on Ground Penetrating Radar Phenomics. *Remote Sens.* **2021**, *18*, 4908. [\[CrossRef\]](#)
- Carmela, R.; Belmonte, A.; Quarto, R.; Quarto, F.; Ruggieri, S.; Castrignanò, A. Potential of Gpr Data Fusion with Hyperspectral Data for Precision Agriculture of the Future. *SSRN J.* **2022**, *199*, 107–109. [\[CrossRef\]](#)
- De Aguiar, G.Z.; Lins, L.; De Paulo, M.F.; Maciel, S.T.R.; Rocha, A.A. Dielectric Permittivity Effects in the Detection of Tree Roots Using Ground-Penetrating Radar. *J. Appl. Geophys.* **2021**, *193*, 104435. [\[CrossRef\]](#)
- Parsekian, A.D.; Slater, L.; Schäfer, K.V.R. Small Root Biomass Effect on the Dielectric Properties of Soil. *Vadose Zone J.* **2012**, *11*, vzt2011.0049. [\[CrossRef\]](#)
- Everett, M.E. *Near-Surface Applied Geophysics*; Cambridge University Press: Cambridge, UK; New York, NY, USA, 2014; ISBN 978-1-107-01877-8.
- Utsi, E.C. *Ground Penetrating Radar*, 1st ed.; Elsevier: Boston, MA, USA, 2017; ISBN 978-0-08-102216-0.
- Barton, C.V.M.; Montagu, K.D. Detection of Tree Roots and Determination of Root Diameters by Ground Penetrating Radar under Optimal Conditions. *Tree Physiol.* **2004**, *24*, 1323–1331. [\[CrossRef\]](#)
- Gimode, D.; Chu, Y.; Holbrook, C.C.; Fonceka, D.; Porter, W.; Dobreva, I.; Teare, B.; Ruiz-Guzman, H.; Hays, D.; Ozias-Akins, P. High-Throughput Canopy and Belowground Phenotyping of a Set of Peanut CSSLs Detects Lines with Increased Pod Weight and Foliar Disease Tolerance. *Agronomy* **2023**, *13*, 1223. [\[CrossRef\]](#)
- Javadi, M.; Ghasemzadeh, H. Wavelet Analysis for Ground Penetrating Radar Applications: A Case Study. *J. Geophys. Eng.* **2017**, *14*, 1189–1202. [\[CrossRef\]](#)
- Ma, Y.; Jong, Y.; Liu, Y. A New De-Noising Method for Ground Penetrating Radar Signal. *J. Phys.* **2020**, *7*, 022002. [\[CrossRef\]](#)
- Wutke, M.; Lejzerowicz, A.; Garbacz, A. The Use of Wavelet Analysis to Improve the Accuracy of Pavement Layer Thickness Estimation Based on Amplitudes of Electromagnetic Waves. *Materials* **2020**, *18*, 3214. [\[CrossRef\]](#)
- Zhang, S.; Zhang, L.; Ling, T.; Fu, G.; Guo, Y. Experimental Research on Evaluation of Soil Water Content Using Ground Penetrating Radar and Wavelet Packet-Based Energy Analysis. *Remote Sens.* **2021**, *13*, 5047. [\[CrossRef\]](#)
- Jessup, R.W.; Klein, R.R.; Burson, B.L.; Murray, S.C.; Washburn, J.D.; Heitholt, J.J.; Foster, J.L. Registration of Perennial *Sorghum Bicolor* × *S. Propinquum* Line PSH12TX09. *J. Plant Regist.* **2017**, *11*, 76–79. [\[CrossRef\]](#)

29. Xiong, S.; Kätterer, T. Carbon-Allocation Dynamics in Reed Canary Grass as Affected by Soil Type and Fertilization Rates in Northern Sweden. *Acta Agric. Scand. Sect. B-Soil Plant Sci.* **2010**, *60*, 24–32. [\[CrossRef\]](#)
30. Kim, K.; Scott, W.R. Design of a Resistively Loaded Vee Dipole for Ultrawide-Band Ground-Penetrating Radar Applications. *IEEE Trans. Antennas Propagat.* **2005**, *53*, 2525–2532. [\[CrossRef\]](#)
31. Nuzzo, L.; Alli, G.; Guidi, R.; Cortesi, N.; Sarri, A.; Manacorda, G. A New Densely-Sampled Ground Penetrating Radar Array for Landmine Detection. In Proceedings of the 15th International Conference on Ground Penetrating Radar, Brussels, Belgium, 30 June–4 July 2014; pp. 969–974.
32. Montoya, T.P.; Smith, G.S. Resistively-Loaded Vee Antennas for Short-Pulse Ground Penetrating Radar. In Proceedings of the IEEE Antennas and Propagation Society International Symposium, Baltimore, MD, USA, 21–26 July 1996; Volume 3, pp. 2068–2071.
33. Shen, X.; Foster, T.; Baldi, H.; Dobрева, I.; Burson, B.; Hays, D.; Tabien, R.; Jessup, R. Quantification of Soil Organic Carbon in Biochar-Amended Soil Using Ground Penetrating Radar (GPR). *Remote Sens.* **2019**, *11*, 2874. [\[CrossRef\]](#)
34. Diamanti, N.; Annan, A.P. Air-Launched and Ground-Coupled GPR Data. In Proceedings of the 2017 11th European Conference on Antennas and Propagation (EUCAP), Paris, France, 19–24 March 2017; pp. 1694–1698.
35. Cassidy, N. Ground Penetrating Radar Data Processing, Modelling and Analysis. In *Ground Penetrating Radar*; Elsevier: Amsterdam, The Netherlands, 2009; pp. 141–176, ISBN 978-0-444-53348-7.
36. Quadfeul, S.-A.; Aliouane, L. Multiscale Analysis of 3D GPR Data Using the Continuous Wavelet Transform. In Proceedings of the XIII International Conference on Ground Penetrating Radar, Lecce, Italy, 21–25 June 2010; pp. 1–4.
37. Savelyev, T.G.; Sato, M. Comparative Analysis of UWB Deconvolution and Feature-Extraction Algorithms for GPR Landmine Detection. In *Detection and Remediation Technologies for Mines and Minelike Targets IX*; Harmon, R.S., Broach, J.T., Holloway, J.H., Jr., Eds.; SPIE: Orlando, FL, USA, 2004; p. 1008.
38. Liu, X.; Dong, X.; Leskovar, D.I. Ground Penetrating Radar for Underground Sensing in Agriculture: A Review. *Int. Agrophys.* **2016**, *30*, 533–543. [\[CrossRef\]](#)
39. Wernette, P.; Houser, C.; Weymer, B.A.; Everett, M.E.; Bishop, M.P.; Reece, B. Influence of a Spatially Complex Framework Geology on Barrier Island Geomorphology. *Mar. Geol.* **2018**, *398*, 151–162. [\[CrossRef\]](#)
40. Morlet, J.; Arens, G.; Fourgeau, E.; Glard, D. Wave Propagation and Sampling Theory—Part I: Complex Signal and Scattering in Multilayered Media. *Geophysics* **1982**, *47*, 203–221. [\[CrossRef\]](#)
41. Morlet, J.; Arens, G.; Fourgeau, E.; Giard, D. Wave Propagation and Sampling Theory—Part II: Sampling Theory and Complex Waves. *Geophysics* **1982**, *47*, 222–236. [\[CrossRef\]](#)
42. Virtanen, P.; Gommers, R.; Oliphant, T.E.; Haberland, M.; Reddy, T.; Cournapeau, D.; Burovski, E.; Peterson, P.; Weckesser, W.; Bright, J.; et al. SciPy 1.0: Fundamental Algorithms for Scientific Computing in Python. *Nat. Methods* **2020**, *17*, 261–272. [\[CrossRef\]](#) [\[PubMed\]](#)
43. Liu, X.; Dong, X.; Xue, Q.; Leskovar, D.I.; Jifon, J.; Butnor, J.R.; Marek, T. Ground Penetrating Radar (GPR) Detects Fine Roots of Agricultural Crops in the Field. *Plant Soil* **2018**, *423*, 517–531. [\[CrossRef\]](#)
44. Godkin, R. *High Throughput Phenotyping of Above and Belowground Sorghum*; American Geophysical Union: Chicago, IL, USA, 2022.

Disclaimer/Publisher’s Note: The statements, opinions and data contained in all publications are solely those of the individual author(s) and contributor(s) and not of MDPI and/or the editor(s). MDPI and/or the editor(s) disclaim responsibility for any injury to people or property resulting from any ideas, methods, instructions or products referred to in the content.